Robotica (2012) volume 30, pp. 171–184. © Cambridge University Press 2011
doi:10.1017/S0263574711000361

Modeling and experiment of a planar 3-DOF parallel micromanipulator

Yi Yue†, Feng Gao†*, Zhenlin Jin‡ and Xianchao Zhao†

†*State Key Laboratory of Mechanical System and Vibration, Shanghai Jiaotong University, Shanghai 200240, P. R. China*
‡*College of Mechanical Engineering, Yanshan University, Qinhuangdao 066004, P. R. China*

(Received in Final Form: March 21, 2011. First published online: May 19, 2011)

SUMMARY
In this paper, a planar 3-DOF $XY\gamma$ parallel micromanipulator with monolithic structure is presented. The micromanipulator is driven by three piezoelectric (PZT) actuators. To achieve highly accurate control, a new approach investigating the relationship among input-force, payload, stiffness, and displacement (IPSD model) of the $XY\gamma$ micromanipulator is proposed in analytical style, and the analytical expression of the relationship between driving voltages of PZT actuators and outputs of end-effector is deduced based on the IPSD model. Finally, in order to verify the IPSD model, the simulations by finite element method and experiment are performed. The micromanipulator can be used to do microtasks that need the manipulator perform only planar motion, such as microoperation and microassembly, and the proposed IPSD model is useful for both digital control and design of the $XY\gamma$ micromanipulator.

KEYWORDS: Compliant mechanisms; Parallel micromanipulator; Stiffness; Flexure hinge.

1. Introduction

As a fusion of parallel mechanism[1] and compliant mechanism,[2] a compliant parallel mechanism (CPM) possesses the advantages of the two types of mechanisms. So, a CPM is employed as an ultraprecision manipulation system in various fields, such as fiber optic coupling, microgrippers, scanning electron microscopy, microlithography, and semiconductor with the advantages of no error accumulation, no backlash, no friction, no need for lubrication, higher mechanical stiffness, higher loading capacity, and higher positioning accuracy.

In 1978, Scire and Teague[3] developed one of the earliest compliant micromotion stages for use in electron microscopes. In 1988, Hudgens and Tesar[4] made a fully parallel 6-DOF micromanipulator with flexure hinges, which could be used in error compensation and force control. After that, in order to apply in different domains, many micromanipulators had been developed. Gao *et al.*[5] designed a 2-DOF piezo-driven precision micromanipulator utilizing flexure hinges. Xu and Li[6] studied an *XY* micromanipulator with two flexure kinematic chains, and each of them consists of a parallelogram structure including four flexure revolute (R) hinges and a flexure prismatic (P) hinge in sequence. Yao *et al.*[7,8] presented an *XYZ* nanopositioning stage with three independent chains, and each chain was comprised of two flexure parallelogram four-bar mechanisms. H. Pham and I. Chen,[9] X. Tang *et al.*,[10] and Y. Yue *et al.*[11] studied the *XYZ* CPMs with perpendicular structure, respectively. In ref. [9], each kinematic chain (P-3-RRR) was comprised of a flexure P-hinge and a flexure chain group (3-RRR). In ref. [10], each kinematic chain (PPP) was composed of three flexure P-hinges. In ref. [11], each kinematic chain (PP^S) was made up of a flexure P-hinge and a spatial parallelogram four-bar mechanism (P^S) with four flexure spherical (S) hinges. P. Gao and S.-M. Swei[12] proposed a 6-DOF micromanipulator in which the upper platform and lower platform were connected by three flexure RPS chains, and the lower platform was comprised of three flexure RPR chains. Y. Yue *et al.*[13] presented a 6-DOF micromanipulator with perpendicular structure in which the six chains were divided into three identical groups, and the actuating directions in different group were normal to each other.

In recent years, the study of planar micromanipulator has attracted much attention and the results in this subject are abundant. G. Chung and K. Choi[14] designed a flexure 3-PPR micromanipulator, and the direct kinematics was deduced. T. Lu *et al.*[15–17] designed a 3-RRR planar micromanipulator consisting of a monolithic mechanism with piezoelectric (PZT) actuators, the kinematic model and the closed-form output compliance model of the manipulator were derived. B. Yi *et al.*[18] also studied the planar 3-RRR micromanipulator. To guarantee the positioning accuracy of the planar micromanipulator, each flexure R-hinge was modeled as a 2-DOF flexure hinge, and the simulation and experiment were performed to show the effectiveness of the model. Though researchers have proposed some planar micromanipulators, such as 3-PPR and 3-RRR, most of them could not provide kinematic decoupling motions, and most papers concerning CPMs focus on the kinematics, such as workspace, dexterity, and accuracy, while less attention has been paid to the relationship among input-force, payload, stiffness, and displacement (IPSD model) of CPM.

Piezo actuators can only provide linear motion with one traditional DOF. To design a multi-DOF micromanipulator with higher mechanical stiffness and higher loading capacity, especially to obtain the rotational DOF, it is better to apply parallel structure. In this paper, we propose a new planar

* Corresponding author. E-mail: fengg@sjtu.edu.cn

https://doi.org/10.1017/S0263574711000361 Published online by Cambridge University Press

3-DOF $XY\gamma$ parallel micromanipulator, which is driven by PZT actuators. The micromanipulator is designed with monolithic structure, and the micromanipulator has the kinematic decoupling characteristic. The analytical IPSD model is derived, and the analytical expression of the relationship between driving voltages of PZT actuators and outputs of end-effector is deduced based on the IPSD model. Moreover, the Cartesian stiffness matrix and the driven stiffness matrix of the $XY\gamma$ micromanipulator are obtained. Finally, the simulations by finite element method (FEM) and experiments are performed to verify the IPSD model.

The paper includes nine sections. The remaining sections are organized as follows: section 2 gives the description of the structure of the planar $XY\gamma$ micromanipulator. Section 3 discusses the kinematic decoupling characteristic of the micromanipulator. In Section 4, the IPSD model is founded, and the kinematic constraint equations are derived. Section 5 gives the analytical IPSD expression and stiffness matrix of the planar micromanipulator. Section 6 deduces the relationship between driving voltages of PZT actuators and outputs of end-effector based on the IPSD model. Section 7 performs simulations by FEM. Section 8 shows experimental results and discussion. Section 9 is conclusion.

2. Structure of the Planar Micromanipulator

A planar 3-DOF $XY\gamma$ parallel micromechanism is proposed and shown in Fig. 1. It is a monolithic compliant mechanism utilizing flexure hinges. The end-effector is connected to the base by three compliant PRR chains. The main structure includes base, end-effector, and three PRR chains. Each PRR chain is driven by one PZT actuator. The three actuators in the micromanipulator are divided into two groups: group 1 has one PRR chain; group 2 has two PRR chains. The actuated directions of group 1 and group 2 are normal to each other. Figure 2 indicates the prototype of the planar $XY\gamma$ micromanipulator. Figure 3 depicts one PRR chain of the structure with integrated flexure hinges. Each PRR chain contains one flexure double parallel plate P-hinge (Fig. 5), two flexure R-hinges (Fig. 4), and one PZT actuator. Figures 4 and 5 show the geometries of flexure P-hinges and flexure R-hinges.

As illustrated in Figs. 2–5, the planar micromanipulator is composed of base, end-effector, linkages, P-hinges, R-hinges, pretighten device, and PZT actuators. The base, end-effector, pretighten device, and all linkages are regarded as rigid. P-hinge has one translational DOF along axis 1, and R-hinge allows rotations about the axis Z. K_1 is the translational stiffness along axis 1.K_z is the rotational stiffness about Z-axis. These stiffness are calculated as following :[19,20]

$$K_1 = 2\frac{2Ebt^3}{s^3}, \tag{1}$$

$$K_Z = \frac{Ee}{\int_0^{\pi}\left(\frac{12R\sin\theta}{(2R+p-2R\sin\theta)^3}\right)\mathrm{d}\theta}, \tag{2}$$

where E is the Young's modulus; b, t, and s are the geometrical parameters of flexure P-hinge (Fig. 5); R, e, p, and θ are the geometrical parameters of flexure R-hinge (Fig. 4).

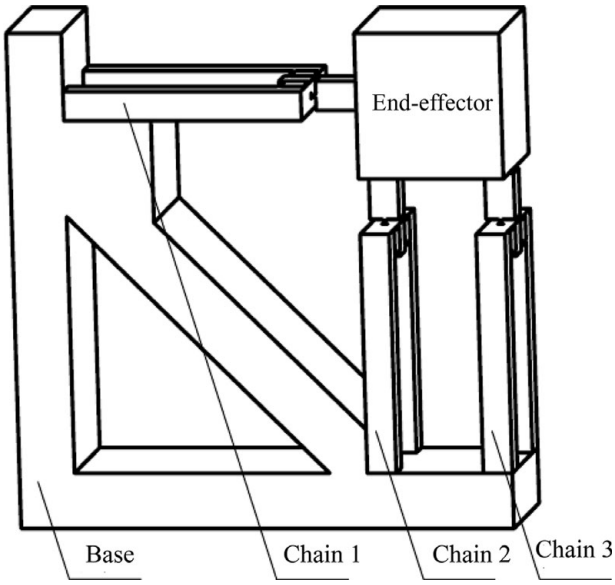


Fig. 1. The 3-PRR mechanism.

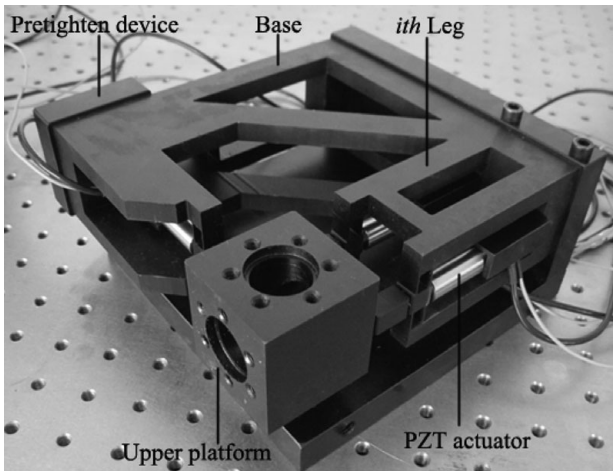


Fig. 2. The prototype of 3-PRR micromanipulator.

3. Kinematic Decoupling Characteristic of the Planar Micromanipulator

In the following statement, $i(i = 1, 2, 3)$ represents one of the three chains. A mechanism sketch of the planar 3-DOF micromanipulator is given in Fig. 6. The center of the R-hinge in each of the three PRR chains connected to the end-effector is denotes asA_i, and the center of the R-hinge in each of the three PRR chains connected to the base by a P-hinge is denoted as C_i. A fixed global coordinate system Ж:o-xyz is located at the center of the end-effector with the X-axis directed along C_1A_1 and Y-axis paralleled C_3A_3. A reference coordinate system Ж:$o - x'y'z'$ is also located at the center of end-effector, and it is coincident with the fixed coordinate system at initial position. Related geometric parameters are $A_2A_3 = 2d$, $C_iA_i = L$, $o'A_i = a$. The displacement

https://doi.org/10.1017/S0263574711000361 Published online by Cambridge University Press

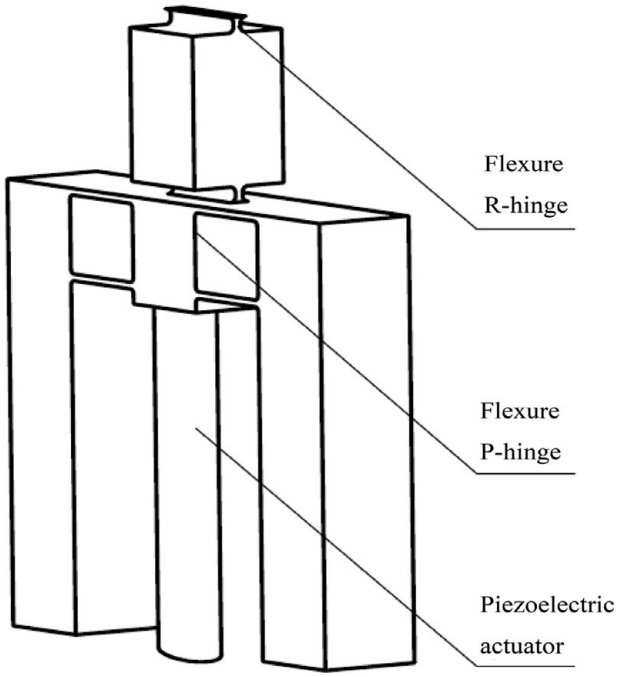


Fig. 3. PRR chain with flexure hinges.

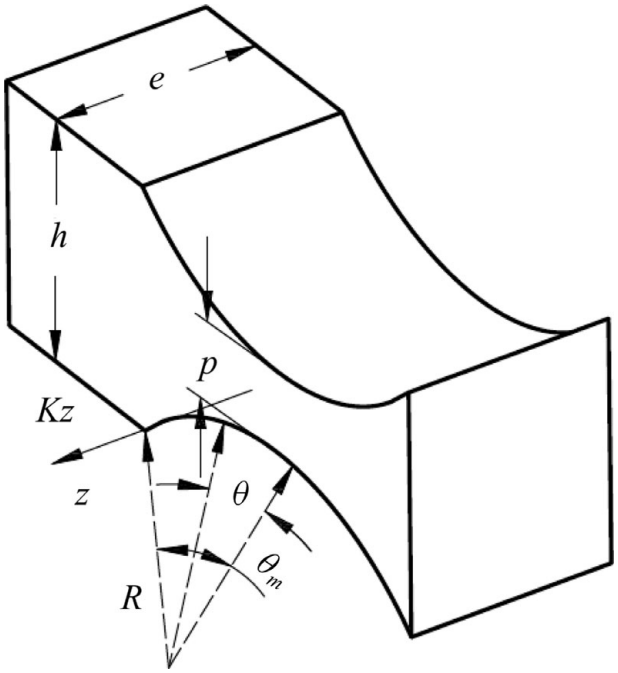


Fig. 4. Flexure R-hinge.

equation of the parallel manipulator is

$$(X_{C_i} - X_{A_i})^2 + (Y_{C_i} - Y_{A_i})^2 + (Z_{C_i} - Z_{A_i})^2 = L^2, \quad (3)$$

where subscripts C_i and A_i denote the three-dimensional position vectors of point C_i and A_i, respectively. Then, we can obtain the inverse kinematics solution by using Eq. (3) as

$$q_1 = am + x + L - \sqrt{L^2 - (a\sin(\gamma) + y)^2}, \quad (4)$$

$$q_2 = am - d\sin(\gamma) + y + L - \sqrt{L^2 - (a\sin(\gamma) + \mathrm{d}m + x)^2}, \quad (5)$$

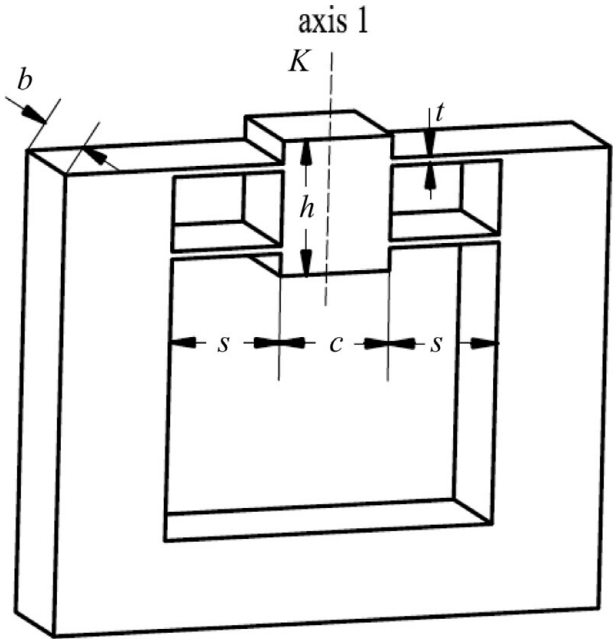


Fig. 5. Flexure double parallel plate P-hinge.

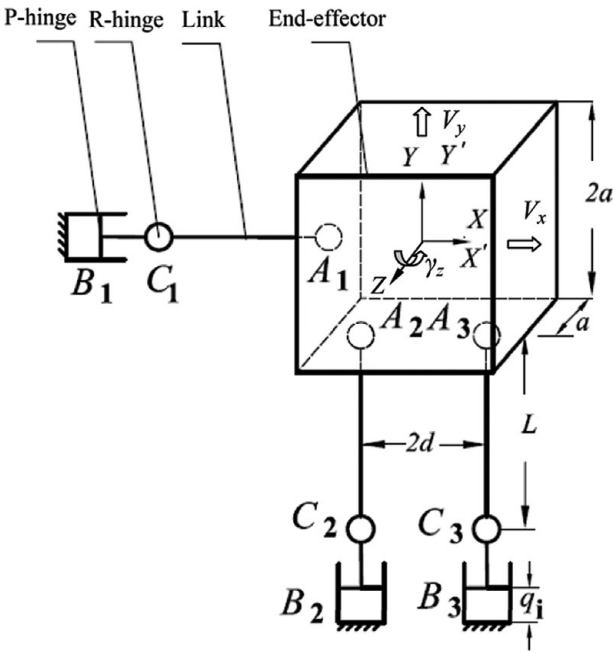


Fig. 6. The mechanical sketch of 3-PRR micromanipulator.

$$q_3 = am + d\sin(\gamma) + y + L - \sqrt{L^2 - (a\sin(\gamma) - \mathrm{d}m + x)^2}, \quad (6)$$

where $m = 1 - \cos(\gamma)$. q_i is the input displacement of the ith P-hinge. Eqs. (4)–(6) can be differentiated with respect to time to obtain the velocity equations, and the velocity equations can be described as following:

$$\dot{q} = A\dot{p}, \quad (7)$$

where $\dot{q}$ is the vector of input velocities defined as

$$\dot{q} = [\dot{q}_1 \quad \dot{q}_2 \quad \dot{q}_3]^{\mathrm{T}}. \quad (8)$$

https://doi.org/10.1017/S0263574711000361 Published online by Cambridge University Press

$\dot{p}$ is the vector of output velocities defined as

$$\dot{p} = [\dot{x}\ \dot{y}\ \dot{\gamma}\ ]^{\mathrm{T}}. \tag{9}$$

A is a 3×3 matrix

$$A = \begin{bmatrix} 1 & \dfrac{a\sin(\gamma)+y}{\sqrt{L^2-(a\sin(\gamma)+y)^2}} & a\sin(\gamma)+\dfrac{(a(a\sin(\gamma)+y)\cos(\gamma))}{\sqrt{L^2-(a\sin(\gamma)+y)^2}} \\ \dfrac{a\sin(\gamma)+\mathrm{d}m+x}{\sqrt{L^2-(a\sin(\gamma)+\mathrm{d}m+x)^2}} & 1 & n_1+\dfrac{n_2(a\sin(\gamma)+\mathrm{d}m+x)}{\sqrt{L^2-(a\sin(\gamma)+\mathrm{d}m+x)^2}} \\ \dfrac{a\sin(\gamma)+\mathrm{d}m)+x}{\sqrt{L^2-(a\sin(\gamma)-\mathrm{d}m+x)^2}} & 1 & p_1+\dfrac{p_2(a\sin(\gamma)+\mathrm{d}m+x)}{\sqrt{L^2-(a\sin(\gamma)-\mathrm{d}m+x)^2}} \end{bmatrix}, \tag{10}$$

where

$$\begin{aligned} n_1 &= a\sin(\gamma) - d\cos(\gamma), \\ n_2 &= a\cos(\gamma) + d\sin(\gamma), \\ p_1 &= a\sin(\gamma) + d\cos(\gamma), \\ p_2 &= a\cos(\gamma) - d\sin(\gamma). \end{aligned}$$

By Eq. (7), we can get

$$\dot{p} = J\dot{q} = A^{-1}\dot{q}, \tag{11}$$

where J is the Jacobian matrix of the manipulator, and we have

$$J = A^{-1}. \tag{12}$$

Obviously, the manipulator will be under architecture singularity if $C_iA_i(i = 1, 2, 3)$ is parallel to each other.[21] Meanwhile, the length of linkage L_i should be equal to the input displacement q_i of the ith P-hinge, and the rotational angle γ is equal to zero. When the 3-PRR mechanism is used as micromanipulator, the length of linkage L_i is much larger than the input displacement q_i. So, the trajectory is singularity-free in its workspace.

For the micromanipulator proposed in this paper, in the initial position, where $x = y = \gamma = 0$, from Eqs. (10) and (12), we get[22]

$$A = \begin{bmatrix} 1 & 0 & 0 \\ 0 & 1 & -d \\ 0 & 1 & d \end{bmatrix}, \tag{13}$$

$$J = \begin{bmatrix} 1 & 0 & 0 \\ 0 & \dfrac{1}{2} & \dfrac{1}{2} \\ 0 & -\dfrac{1}{2d} & \dfrac{1}{2d} \end{bmatrix}. \tag{14}$$

Because the dimensions of translational velocity and angular velocity are different, Eq. (11) has to be rewritten as

$$V = J_v\dot{q}, \tag{15}$$

$$\omega = J_\omega\dot{q}, \tag{16}$$

where J_v and J_ω are the matrices consisting of lines 1–2 and lines 3 of matrix J, respectively. Therefore, we can obtain the following results:

$$J_vJ_v^{\mathrm{T}} = diag\begin{pmatrix} 1 & \dfrac{1}{2} \end{pmatrix}, \tag{17}$$

$$J_\omega J_\omega^{\mathrm{T}} = diag\left(\frac{1}{2d^2}\right), \tag{18}$$

$$JJ^{\mathrm{T}} = diag\begin{pmatrix} 1 & \dfrac{1}{2} & \dfrac{1}{2d^2} \end{pmatrix}. \tag{19}$$

According to refs. [23, 24], we can get the conclusion that the planar micromanipulator has the kinematic decoupling characteristic.

4. IPSD Model and Kinematic Constraint Equations

The outputs of actuated pairs of CPMs are affected by not only actuators, but also elastic reaction forces and moments exerted on them. Therefore, the research on the relationship among force, stiffness, and displacement is very important for the design of workspace, the analysis of kinematics and dynamics.

According to the principle of virtual work, we can obtain the following equation:

$$T^{\mathrm{T}} \cdot \delta q + \begin{pmatrix} F \\ M_Z \end{pmatrix}^{\mathrm{T}} \cdot \delta p = \sum_{i=1}^{3} \Delta\phi_i^{\mathrm{T}} \cdot K_i \cdot \delta\phi_i \tag{20}$$

in which

$$T = [T_1 \quad T_2 \quad T_3\ ]^{\mathrm{T}}, \tag{21}$$

$$F = [F_x \quad F_y\ ]^{\mathrm{T}}, \tag{22}$$

$$K_i = diag(k_{qi} \quad k_{C_i} \quad k_{A_i}), \tag{23}$$

where T_i is the input force exerted at the P-hinge of the ith chain. F_x and F_y are the external forces applied at the center of end-effector. M_z is the external moment about Z-axis. K_i is the stiffness vector with respect to $\Delta\Phi_i$, and $\Delta\Phi_i$ would be described in Section 4.2. δq, δp, and $\Delta\Phi_i$ are the virtual displacements of PZT actuators, end-effector, and the flexure hinges of the ith chain, respectively.

In order to deduce analytic expressions of the IPSD model, the kinematic constraint equations of the manipulator and each kinematic chain should be deduced first. There are two kinds of kinematic constraint equations for parallel

https://doi.org/10.1017/S0263574711000361 Published online by Cambridge University Press

micromanipulator: one gives the geometrical restriction between the outputs of end-effector and all inputs of actuators; another gives the geometrical restriction between outputs of end-effector and inputs of all kinematic pairs of each chain.

4.1. Kinematic constraint equation of the planar micromanipulator

Because the workspace of micromanipulator is very small, the Jacobian matrix J can be regarded as a constant matrix at initial position.[22] From Eqs. (11) and (14), we can obtain the kinematic constraint equation between outputs and all inputs of actuator as

$$\Delta p = B\Delta q, \tag{24}$$

$$\Delta q = [\Delta q_1 \quad \Delta q_2 \quad \Delta q_3]^{\mathrm{T}}, \tag{25}$$

$$\Delta p = [\Delta x \quad \Delta y \quad \Delta\gamma]^{\mathrm{T}}, \tag{26}$$

$$B = J = \begin{bmatrix} 1 & 0 & 0 \\ 0 & \frac{1}{2} & \frac{1}{2} \\ 0 & -\frac{1}{2d} & \frac{1}{2d} \end{bmatrix}, \tag{27}$$

where Δp is the minute displacement output of end-effector, Δq is the minute displacement input of PZT actuator. Δx, Δy, $\Delta\gamma$ are the translational displacement along X-axis, Y-axis, and the rotational angle about Z-axis, respectively. Δq_i is the input displacement of the ith actuator.

4.2. The kinematic constraint equation of PRR chain

The mechanical sketch of PRR chain is shown in Fig. 7. S_1 denotes the translational axis of P-hinge, $S_j(j = 2, 3)$ denotes the rotational axis of R-joint. Ж:O-xyz and Ж:$O' - x'y'z'$ denote the fixed coordinate system and reference coordinate system of the micromanipulator, respectively. Ж:$O_0 - x_0y_0z_0$ is the local fixed coordinate system of the PRR chain. Then, the displacement equations of the ith chain can be expressed as

$$\Delta D = J_{O_0C_iA_i}\Delta\Omega_{O_0C_iA_i} \tag{28}$$

in which

$$\Delta D = [\Delta x \quad \Delta y \quad \Delta z \quad \Delta\alpha \quad \Delta\beta \quad \Delta\gamma]^{\mathrm{T}}, \tag{29}$$

$$\Delta\Omega_{O_0C_iA_i} = [\Delta q_i \quad \Delta\varphi_{Ci} \quad \Delta\varphi_{Ai}]^{\mathrm{T}}, \tag{30}$$

$$J_{O_0CA} = \begin{bmatrix} S_1 & S_2 \times {}^0P_{o2} & S_3 \times {}^0P_{o2} \\ 0 & S_2 & S_3 \end{bmatrix}, \tag{31}$$

where $\Delta\alpha$ and $\Delta\beta$ are the rotational angle about X-axis and Y-axis, respectively, Δz is the translational displacement along Z-axis. $J_{O_0C_iA_i}$ is the Jacobian matrix of the $O_0C_iA_i$ chain. $\Delta\Omega_{O_0C_iA_i}$ is the displacement input vector of $O_0C_iA_i$ chain. $\Delta\varphi_{Ci}$ and $\Delta\varphi_{Ai}$ are the rotational angle about S_2-axis and S_3-axis, respectively. P_{oj} denotes the position vector from the origin of $o_j - x_jy_jz_j(j = 1, 2, 3)$ to the origin of Ж: $o - x'y'z'$ with respect to Ж: $o - x_0y_0z_0$ of the ith chain.

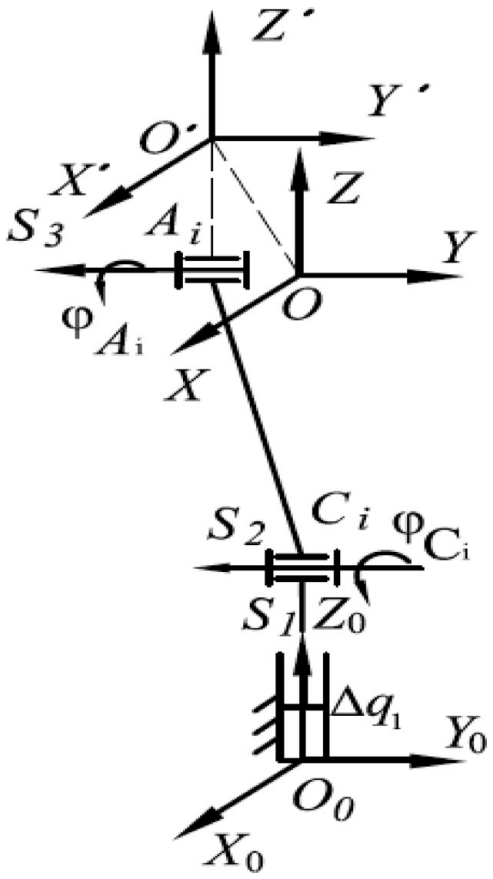


Fig. 7. The mechanical sketch of PRR chain.

The coordinate system $o_j - x_jy_jz_j$ can be obtained by D–H coordinate. For the 3-PRR parallel micromanipulator, there is $\Delta z = \Delta\alpha = \Delta\beta = 0$. After simplification, we get Eq. (32) from Eq. (28)

$$\Delta p = J_i\Delta\phi_i, \tag{32}$$

where J_i and $\Delta\phi_i$ are the Jacobian matrix and the displacement input vector of the ith PRR chain, respectively. According to Eq. (32), the kinematic constraint equation of the ith PRR chain can be writen as

$$\Delta\phi_i = C_i\Delta p, \tag{33}$$

where

$$C_i = J_i^{-1}, \tag{34}$$

and there are

$$C_1 = \begin{bmatrix} L & 0 & 0 \\ 0 & 1 & -a \\ 0 & -1 & a+L \end{bmatrix} \Big/ L, \tag{35}$$

$$C_2 = \begin{bmatrix} 0 & L & -\mathrm{d}L \\ -1 & 0 & -a \\ 1 & 0 & a+L \end{bmatrix} \Big/ L, \tag{36}$$

$$C_3 = \begin{bmatrix} 0 & L & \mathrm{d}L \\ -1 & 0 & -a \\ 1 & 0 & a+L \end{bmatrix} \Big/ L. \tag{37}$$

https://doi.org/10.1017/S0263574711000361 Published online by Cambridge University Press

5. The Analytical Expression of IPSD Model and Stiffness Matrix

In Eq. (20), though $\delta q, \delta p$, and $\delta\phi_i$ are virtual displacements, they have to follow the kinematic constraint Eqs. (24) and (33), and there are

$$\delta p = B\delta q, \delta\phi_i = C_i\delta p, \Delta\phi_i = C_i\Delta p. \tag{38}$$

Substituting δp, $\delta\phi_i$, and $\Delta\phi_i$ in Eq. (38) into (20) and simplifying it, Eq. (20) can be rewritten as follows:

$$T + B^{\mathrm{T}}\begin{pmatrix} F \\ M_Z \end{pmatrix} = \sum_{i=1}^{3}(B^{\mathrm{T}}C_i K_i C_i B)\Delta q. \tag{39}$$

Substituting Eqs. (23), (27), (35)–(37), and (40) into Eq. (39), and make all P-hinges and R-hinges have the same geometrical parameters, then we get the analytical expression of IPSD model as

$$T + B^{\mathrm{T}}\begin{pmatrix} F \\ M_Z \end{pmatrix} = K_Q\Delta q, \tag{40}$$

where

$$K_Q = \sum_{i=1}^{3}\left((C_i B)^{\mathrm{T}}K_i^{\mathrm{T}}C_i B\right) = \begin{bmatrix} k_{q11} & k_{q12} & k_{q13} \\ k_{q21} & k_{q22} & k_{q23} \\ k_{q31} & k_{q32} & k_{q33} \end{bmatrix} \tag{41}$$

in which

$$\begin{aligned}
k_{q11} &= (4k_z + k_q L^2)/L^2, \\
k_{q22} &= (2m1k_z + 2dLk_z + 3m2k_z + 3a^2k_z + 4d^2L^2K_q)/ \\
&\quad (4d^2L^2), \\
k_{q33} &= (2m3k_z - 2dLk_z + 3m2k_z + 3a^2k_z + 4d^2L^2k_q)/ \\
&\quad (4d^2L^2), \\
k_{q12} &= k_{q21} = -(4a + 2L)k_z/(2dL^2), \\
k_{q13} &= k_{q31} = (4a + 2L)k_z/(2dL^2), \\
k_{q23} &= k_{q32} = -(3m2 + 3a^2 - 2d^2)k_z/(4d^2L^2),
\end{aligned}$$

where $m1 = d^2 + 2ad$, $m2 = a^2 + 2aL + L^2$, $m3 = d^2 - 2ad$, K_z are the bending stiffness of R-hinge located at point C_i and A_i, K_q is the translational stiffness of double parallel plate P-joint.

When external force and moment are zero, Eq. (40) can be simplified as follows:

$$T = K_Q\Delta q, \tag{42}$$

where K_Q descripts the relationship between input force vector and the input displacement of P-hinge when there is no external force. We name K_Q as the driven stiffness matrix of the 3-PRR micromanipulator.

From Eq. (24), the following equation can be obtained:

$$\Delta q = B^{-1}\Delta \mathrm{p}, \tag{43}$$

where B^{-1} is the inverse matrix of B. When input force vector T is zero, substituting Eq. (43) into Eq. (40), Eq. (40) can be rewritten as follows:

$$\begin{pmatrix} F \\ M_Z \end{pmatrix} = K\Delta p \tag{44}$$

in which

$$K = \sum_{i=1}^{3}\left(C_i^{\mathrm{T}}K_i C_i\right), \tag{45}$$

where K is the Cartesian stiffness matrix of the planar 3-DOF micromanipulator and it reflects the relationship between external force and the output displacement of end-effector when there is no input force.

Substituting Eq. (43) into Eq. (40), we can obtain

$$\Delta p = BK_Q^{-1}\left(T + B^{\mathrm{T}}\begin{pmatrix} F \\ M_Z \end{pmatrix}\right). \tag{46}$$

Equation (46) can be used to calculate the position of end-effector when input force and payload are given.

6. The Relationship between Driving Voltages and Outputs of End-Effector

Because the planar micromanipulator is driven by PZT actuators, in order to design and control the micromanipulator, we need to investigate the relationship between driving voltages of PZT actuators and outputs of end-effector. According to Eq. (40), we can obtain

$$T = K_Q\Delta q - B^{\mathrm{T}}\begin{pmatrix} F \\ M_Z \end{pmatrix}. \tag{47}$$

According to the ref. [25], the output force T_d of PZT actuator can be calculated by

$$T_d = K_t(\Delta L - \Delta q) \tag{48}$$

in which

$$\Delta L = [\Delta l_1 \quad \Delta l_2 \quad \Delta l_3]^{\mathrm{T}}, \tag{49}$$

$$K_t = diag(k_{t1}\ k_{t2}\ k_{t3}), \tag{50}$$

where Δl_i and k_{ti} denote nominal output displacement and stiffness of the ith PZT actuator, respectively. When T_d is equal to T, from Eqs. (47) and (48), we get

$$\Delta L = K_t^{-1}\left((K_t + K_Q)\Delta q - J^{\mathrm{T}}\begin{pmatrix} F \\ M_Z \end{pmatrix}\right), \tag{51}$$

where K_t^{-1} is the inverse matrix of K_t. The driving voltage values can be calculated as

$$U = (\Delta L./\Delta L_0)U_{\max}, \tag{52}$$

https://doi.org/10.1017/S0263574711000361 Published online by Cambridge University Press

where the operator ./ is designed to give element by element division

$$U = [u_1 \quad u_2 \quad u_3]^{\mathrm{T}}, \tag{53}$$

$$U_{\max} = diag(u_{1\max} \quad u_{2\max} \quad u_{3\max}), \tag{54}$$

$$\Delta L_0 = [\Delta l_{10} \quad \Delta l_{20} \quad \Delta l_{30}]^{\mathrm{T}}, \tag{55}$$

where u_i is the driving voltage value of the ith PZT actuator. $u_{i\max}$ denotes the maximum nominal voltage value of the ith actuator. Δl_{i0} means the maximum nominal displacement without external forces or restraints. Substituting ΔL in Eq. (51) into Eq. (52), we can obtain

$$U = \left(\left(K_t^{-1}(K_t + K_Q)\Delta q - J^{\mathrm{T}}F\right)./\Delta L_0\right) U_{\max}. \tag{56}$$

Substituting Eq. (43) into Eq. (56), we get

$$U = \left(\left(K_t^{-1}(K_t + K_Q)J^{-1}\Delta p - B^{\mathrm{T}}\begin{pmatrix} F \\ M_Z \end{pmatrix}\right)./\Delta L_0\right) U_{\max}. \tag{57}$$

Equation (56) expresses the relationship between inputs of P-hinges and driving voltages of PZT actuators. Equation (57) denotes the relationship between outputs of end-effector and driving voltages of PZT actuators.

7. Simulations

To verify the IPSD model of the planar $XY\gamma$ micromanipulator proposed in this paper, simulations by FEM software are performed. When given payload and input force vector, the outputs of end-effector can be calculated by Eq. (46). Then, the payload and the input force vector are applied to a virtual model in the FEM environment. By comparing the outputs of end-effector between the FEM model and the calculated results by Eq. (46), the correctness and effectiveness of the IPSD model can be verified.

Assuming the external force F and external moment Mz are zero, we simulate the translation along X-axis, Y-axis, and the rotation about Z-axis. The given workspaces of translation along X-axis, Y-axis, and rotation about Z-axis are 0–10 μm, 0–10 μm, and 0–0.25 mrad, respectively. The FEM model is shown in Fig. 8. The material properties, stiffness parameters of flexure hinges, and the parameters of PZT actuator are shown in Table I. The comparisons between the simulation data by FEM and the IPSD data by Eq. (46) are shown in Figs. 9–11 and Tables II–IV from which we can find the following:

- When end-effector translates along X-axis: chain 1 should offer a input force T_1 to drive the micromanipulator in functional direction; chains 2 and 3 should offer a moment $d(T_2 - T_3)$ to restrict the rotation about Z-axis, though the γ-output is zero; The force $T_2 + T_3$ should be zero to ensure there is no y-output (Table II and Fig. 9b).
- When end-effector translates along Y-axis: the input force T_1 should be zero to ensure there no x-output; chains 2 and 3 should offer a force $2T_2$ to drive the micromanipulator in functional direction and a moment $d(T_2 - T_3)$ to restrict the rotation about Z-axis, though the γ-output is zero (Table III and Fig. 10b).
- When end-effector rotates about Z-axis: the input force T_1 should be offered to restrict the translation along X-axis; chains 2 and 3 should offer a force $T_2 - T_3$ to restrict the translation along Y-axis and a moment $2T_2d$ to drive the micromanipulator in functional direction (Table IV and Fig. 11b).

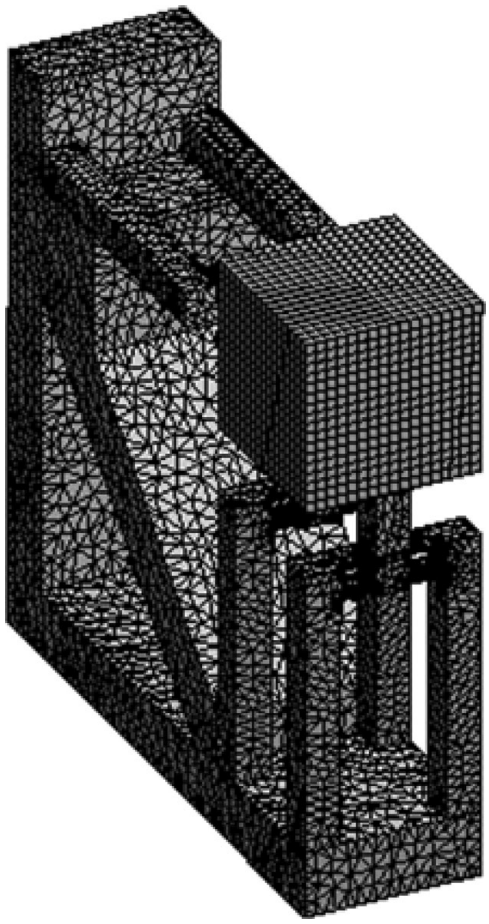


Fig. 8. FEM model.

The results of simulations show negligible errors in nonfunctional directions, and the maximum errors of translation along X-axis, Y-axis, and rotation about Z-axis reach 2.0, 4.63, and 5.60% in functional directions, respectively. Therefore, it is confirmed that the results calculated based on the IPSD model are coincident to the results of simulations by FEM.

8. Experimental Verification

8.1. Experimental setup

The experimental system of the 3-DOF $XY\gamma$ micromanipulator has been developed as shown in Fig. 12. The system consists of a 3-DOF planar micromanipulator, three PZT actuators (P-841.30), D/A card (PCI-6208), control system and measuring equipment. The manipulator is machined by electrospark wire-electrode cutting, and the material is spring

https://doi.org/10.1017/S0263574711000361 Published online by Cambridge University Press

Table I. Material properties, structural parameter, and stiffness parameters.

a	d	$s = b$	$t = R = p$	E	L	k_{ti}	$U_{i\max}$	Δl_{i0}	K_z	K_{qi}
25 mm	20 mm	10 mm	0.8 mm	209 Gpa	19 mm	19 N/μm	100 V	45 um	106 Nm/rad	4.22 N/μm

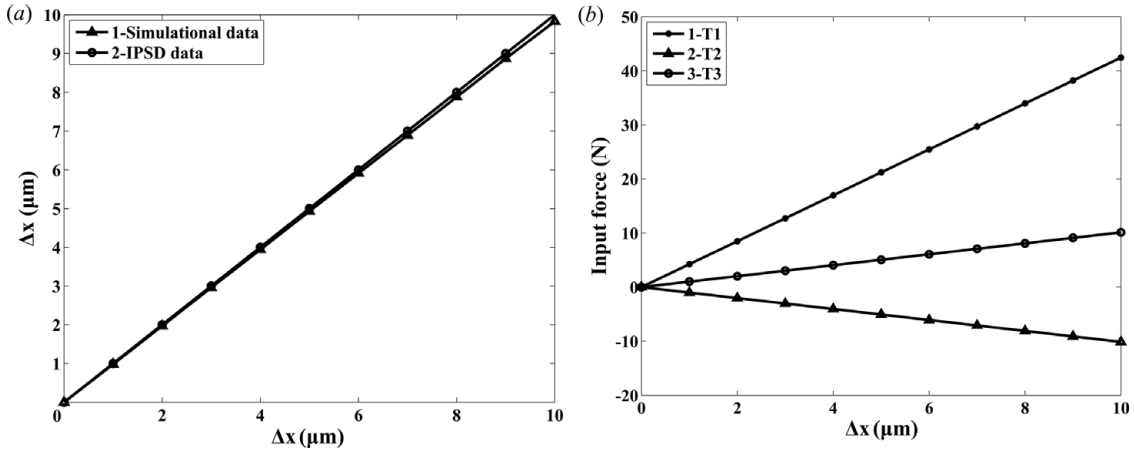


Fig. 9. Comparison of translation along X-axis between FEM and IPSD model. (a) Comparison of translation along X-axis; (b) Relation between input force and Δx-output.

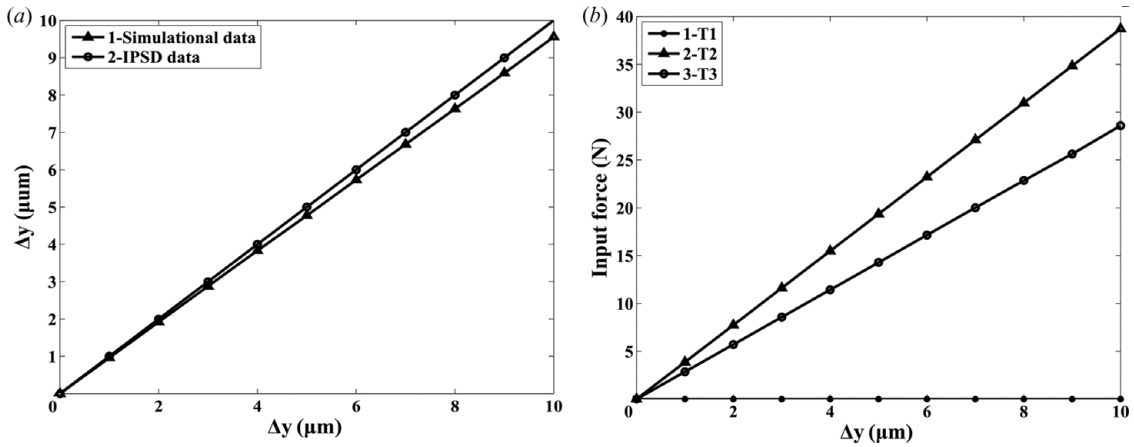


Fig. 10. Comparison of translation along Y-axis between FEM and IPSD model. (a) Comparison of translation along Y-axis; (b) Relation between input force and Δy-output.

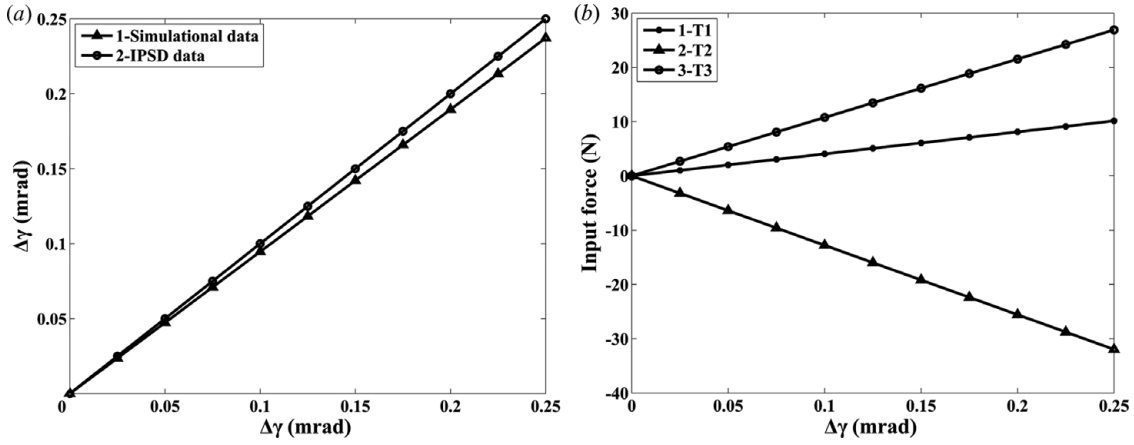


Fig. 11. Comparison of rotation about Z-axis between FEM and IPSD model. (a) Comparison of rotation about Z-axis; (b) Relation between input force and $\Delta\gamma$-output.

https://doi.org/10.1017/S0263574711000361 Published online by Cambridge University Press

Table II. The simulation data when end-effector translates along *X*-axis.

$(F^{\mathrm{T}} \quad M_z^{\mathrm{T}})^{\mathrm{T}} = [0 \quad 0 \quad 0]^{\mathrm{T}}$					$\Delta p = [0 \quad \Delta x \quad 0 \quad 0]^{\mathrm{T}}$		
Input force (*N*)			IPSD data (μm)	Error (%)	The simulational results		
T_1	T_2	T_3	Δz	$\frac{\lvert\Delta x' - \Delta x\rvert}{\Delta x} \times 100$	$\Delta x'$(um)	$\Delta y'$(nm)	$\Delta\gamma'$(urad)
4.25	−1.01	1.01	1	2.00	0.98	9	0.64
8.49	−2.02	2.02	2	1.50	1.97	17	0.91
12.74	−3.04	3.04	3	1.33	2.96	27	1.57
16.98	−4.05	4.05	4	1.50	3.94	31	2,04
21.23	−5.06	5.06	5	1.40	4.93	45	2.38
25.47	−6.08	6.08	6	1.50	5.91	66	2.75
29.72	−7.09	7.09	7	1.57	6.89	79	3.10
33.96	−8.10	8.10	8	1.27	7.88	80	3.63
38.21	−9.12	9.12	9	1.44	8.87	91	4.06
42.45	−10.13	10.13	10	1.70	9.83	103	4.48

Table III. The simulation data when end-effector translates along *Y*-axis.

$(F^{\mathrm{T}} \quad M_z^{\mathrm{T}})^{\mathrm{T}} = [0 \quad 0 \quad 0]^{\mathrm{T}}$					$\Delta p = [0 \quad \Delta y \quad 0]^{\mathrm{T}}$		
Input force (*N*)			IPSD data (μm)	Error (%)	The simulational results		
T_1	T_2	T_3	Δy	$\frac{\lvert\Delta y' - \Delta y\rvert}{\Delta y} \times 100$	$\Delta x'$(nm)	$\Delta y'$(um)	$\Delta\gamma'$(urad)
0	3.87	2.86	1	4.00	7	0.96	0.51
0	7.74	5.71	2	4.00	5	1.92	0.96
0	11.61	8.57	3	4.00	12	2.88	1.63
0	15.48	11.43	4	4.25	19	3.83	2,00
0	19.35	14.29	5	4.60	38	4.77	2.50
0	23.22	17.14	6	4.50	31	5.73	2.75
0	27.09	20.00	7	4.57	49	6.68	3.35
0	30.96	22.85	8	4.63	58	7.63	3.78
0	34.83	25.62	9	4.55	69	8.59	4.33
0	38.70	28.58	10	4.40	77	9.56	4.86

Table IV. The simulation data when end-effector platform rotates about *Z*-axis.

$(F^{\mathrm{T}} \quad M_z^{\mathrm{T}})^{\mathrm{T}} = [0 \quad 0 \quad 0]^{\mathrm{T}}$					$\Delta p = [0 \quad 0 \quad \Delta\gamma]^{\mathrm{T}}$		
Input froce (*N*)			IPSD data (μm)	Error (%)	The simulational results		
T_1	T_2	T_3	$\Delta\gamma$(urad)	$\frac{\lvert\Delta\gamma' - \Delta\gamma\rvert}{\Delta\gamma} \times 100$	$\Delta x'$(nm)	$\Delta y'$(nm)	$\Delta\gamma'$(urad)
1.01	−3.20	2.69	25	5.60	9	22	23.6
2.02	−6.40	5.38	50	5.40	9	38	47.3
3.04	−9.60	8.07	75	5.33	10	52	71.0
4.05	−12.79	10.77	100	5.40	11	65	94.6
5.07	−15.99	13.46	125	5.36	13	75	118.3
6.08	−19.19	16.15	150	5.27	12	87	142.1
7.09	−22.39	18.84	175	5.20	17	96	165.9
8.10	−25.58	21.53	200	5.25	12	111	189.5
9.11	−28.78	24.22	225	5.20	15	124	213.3
10.13	−31.98	26.91	250	5.12	13	137	237.2

steel 65Mn. As shown in Fig. 13, after computer processing, the input signal is converted into analog voltage output signal form 0 to 10 V by D/A converter. Then, amplified by the PZT controller, the input analog voltage signal is turned into the voltage signal ranged from 0 to 100 V to drive PZT actuators directly, and further, to drive the micromanipulator. Then, the outputs of end-effector are measured by measuring equipment. Finally, the measure results are shown on screen. Table I shows relative PZT actuator parameters and structural parameters of the experimental system. These

https://doi.org/10.1017/S0263574711000361 Published online by Cambridge University Press

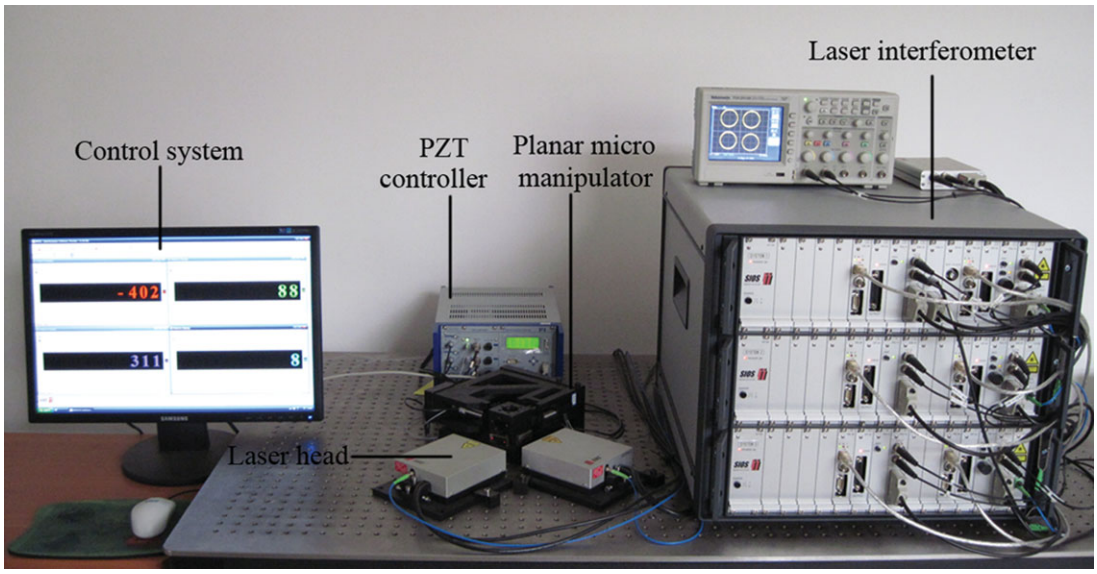


Fig. 12. (Colour Online) The experimental system of the 3-DOF $XY\gamma$ micromanipulator.

stiffness values of flexure hinges are calculated by Eqs. (1) and (2).

The measuring equipment includes two double beam laser interferometers. Each laser interferometer can measure one translational DOF along the laser direction and one rotational DOF in the plane that the two laser beams lie in. By the appropriate layout of laser interferometers, two laser interferometers can measure two translational DOF and two rotational DOF, and three laser interferometers may measure all 6-DOF outputs. The measure principle of laser interferometer is shown as Fig. 14. In Fig. 14, d is the constant distance between the two laser beams, α is the rotational angle. $\Delta 1$ and $\Delta 2$ are the displacements of the reflecting points of the two beams, which are noted as point A and B. s is the displacement of point C, which is the middle point of line AB.

8.2. *Experimental results*

The test process is as following:

- Given payload and the outputs of end-effector, the driving voltage values are calculated by Eq. (57).

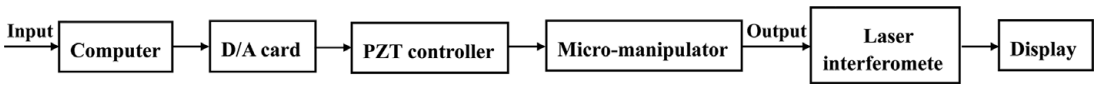


Fig. 13. System flowchart.

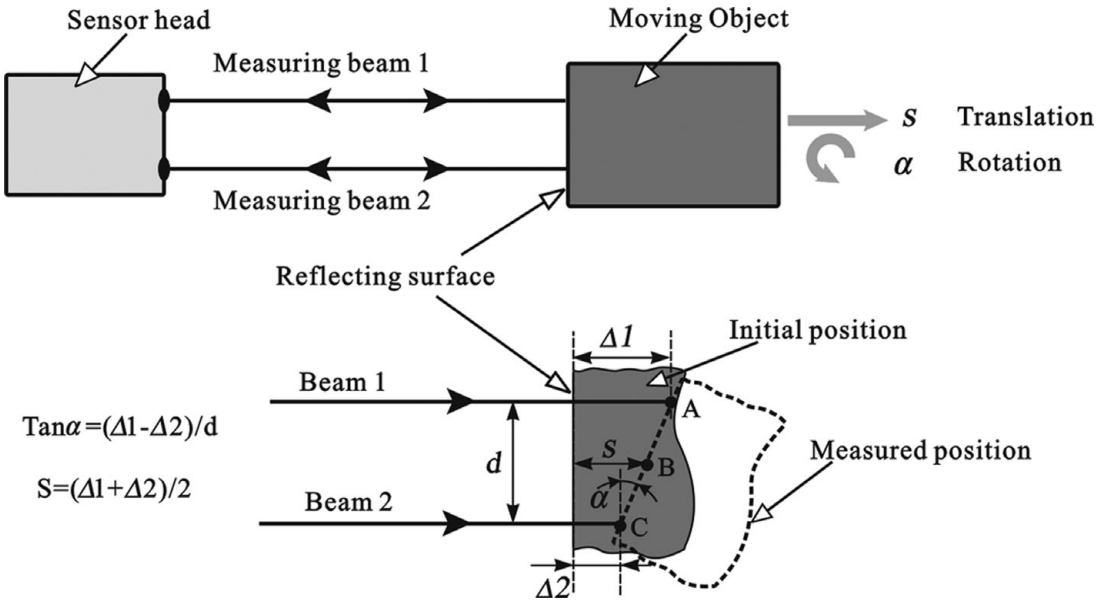


Fig. 14. The measure principle of laser interferometer.

https://doi.org/10.1017/S0263574711000361 Published online by Cambridge University Press

Table V. The experimental data and IPSD data when end-effector moves along *X*-axis.

$(F^{\mathrm{T}} \quad M_z^{\mathrm{T}})^{\mathrm{T}} = [0 \quad 0 \quad 0]^{\mathrm{T}}$					$\Delta \mathrm{X} = [\Delta x \quad 0 \quad 0]^{\mathrm{T}}$		
Driving voltages (V)			IPSD data (μm)	Error (%)	The experimental results		
u_1	u_2	u_3	$\Delta x(um)$	$\frac{\lvert\Delta x' - \Delta x\rvert}{\Delta x} \times 100$	$\Delta x'$(um)	$\Delta y'$(nm)	$\Delta \gamma'$(urad)
2.853	−0.119	0.119	1	7.00	0.930	−42	1
5.706	−0.237	0.237	2	6.85	1.863	−56	1
8.560	−0.355	0.355	3	6.83	2.795	−71	2
11.413	−0.474	0.474	4	6.92	3.723	−83	2
14.267	−0.592	0.592	5	6.56	4.672	−95	3
17.119	−0.711	0.711	6	6.75	5.595	−106	3
19.972	−0.829	0.829	7	6.30	6.559	−118	4
22.825	−0.948	0.948	8	6.24	7.501	−128	5
25.678	−1.066	1.066	9	6.43	8.421	−136	5
28.532	−1.185	1.185	10	6.32	9.368	−147	6

Table VI. The experimental data and IPSD data when end-effector moves along *Y*-axis.

$(F^{\mathrm{T}} \quad M_z^{\mathrm{T}})^{\mathrm{T}} = [0 \quad 0 \quad 0]^{\mathrm{T}}$					$\Delta \mathrm{X} = [0 \quad \Delta y \quad 0]^{\mathrm{T}}$		
Driving voltages (V)			IPSD data (μm)	Error (%)	The experimental result		
u_1	u_2	u_3	$\Delta y(um)$	$\frac{\lvert\Delta y' - \Delta y\rvert}{\Delta y} \times 100$	$\Delta x'$(nm)	$\Delta y'$(um)	$\Delta \gamma'$(urad)
0	2.809	2.691	1	7.80	12	0.922	1
0	5.619	5.382	2	7.60	19	1.848	1
0	8.428	8.073	3	7.47	29	2.776	1
0	11.238	10.767	4	7.78	41	3.689	2
0	14.047	13.455	5	7.38	57	4.631	2
0	16.856	16.145	6	7.22	80	5.567	3
0	19.666	18.836	7	6.93	94	6.515	3
0	22.474	21.527	8	6.98	108	7.442	4
0	25.284	24.218	9	6.82	122	8.386	4
0	28.094	26.909	10	6.87	136	9.313	5

- The driving voltages are acted on the PZT actuators in the experimental environment.
- Using laser interferometer to measure the position and orientation of the micromanipulator.
- Comparing the measure results with the results calculated by the analytic model (Eq. (57)).

In the experimental environment, there is no payload applied on the end-effector, and we don't take the mass of linkages into account. Because PZT actuator cannot produce pull force, the zero point of the $XY\gamma$ micromanipulator is set to X—6 μm, Y—6 μm, γ—0 mrad in the fixed coordinate system, and the driving voltage values of the zero-point are $u_1 = 17.119V$, $u_2 = 16.145V$, and $u_3 = 16.856V$. The given workspaces of translation along X-axis, Y-axis, and rotation about Z-axis are 0–10 μm, 0–10 μm, and 0–0.25 mrad, respectively. The driving voltage values in Figs. 15–17 and Tables V–VII are all relative to the driving voltage values of the zero point.

The experimental results are shown in Figs. 15–17 and Tables V–VII from which we can see that there errors exist between experimental results and IPSD model. The ranges of errors for translation along X-axis, Y-axis, and rotation about Z-axis are 6.24–7.00%, 6.82–7.80%, and 8.44–10.00%, respectively. The cross-coupling errors are not significant; the maximum values of the cross-coupling motion in translation along X-axis, Y-axis, and rotation about Z-axis reach 149 nm, 396 nm, and 0.006 mrad, respectively. When end-effector translates along X-axis, the driving voltage of the first PZT actuator should offer a input force to drive the micromanipulator in functional direction, and the driving voltages of the second and third PZT actuators should offer a moment to restrict the rotation about Z-axis (Table V and Fig. 15b). When end-effector translates along Y-axis, the driving voltage of the first PZT actuator should be zero to ensure there no x-output, and the driving voltages of the second and third PZT actuators should offer a force to drive the micromanipulator in functional direction and a moment to restrict the rotation about Z-axis (Table VI and Fig. 16b). When end-effector rotates about Z-axis, the first, second, and third PZT actuator should offer suited driving voltage values to restrict the translation along X- and Y-axes (Table VII and Fig. 17b).

8.3. Discussion

The experimental results in Table V–VII show that the maximum errors for translation along X-axis, Y-axis, and rotation about Z-axis reach 7.00, 7.80, and 10.0%, respectively, which are closer to simulational results. Since

https://doi.org/10.1017/S0263574711000361 Published online by Cambridge University Press

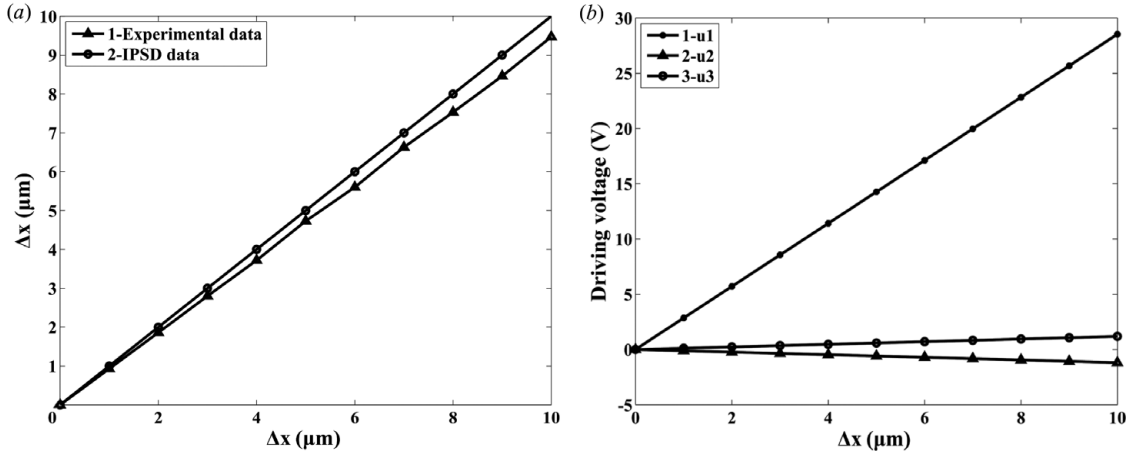


Fig. 15. Comparison of translation along *X*-axis between experimental results and IPSD model. (a) Comparison of translation along *X*-axis; (b) Relation between driving voltages and Δx-output.

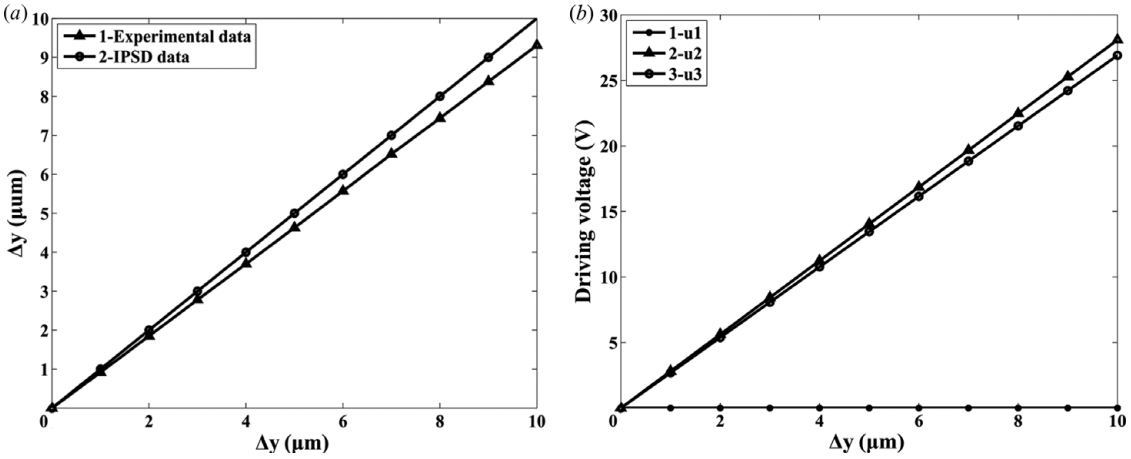


Fig. 16. Comparison of translation along *Y*-axis between experimental results and IPSD model. (a) Comparison of translation along *Y*-axis; (b) Relation between driving voltages and Δy-output.

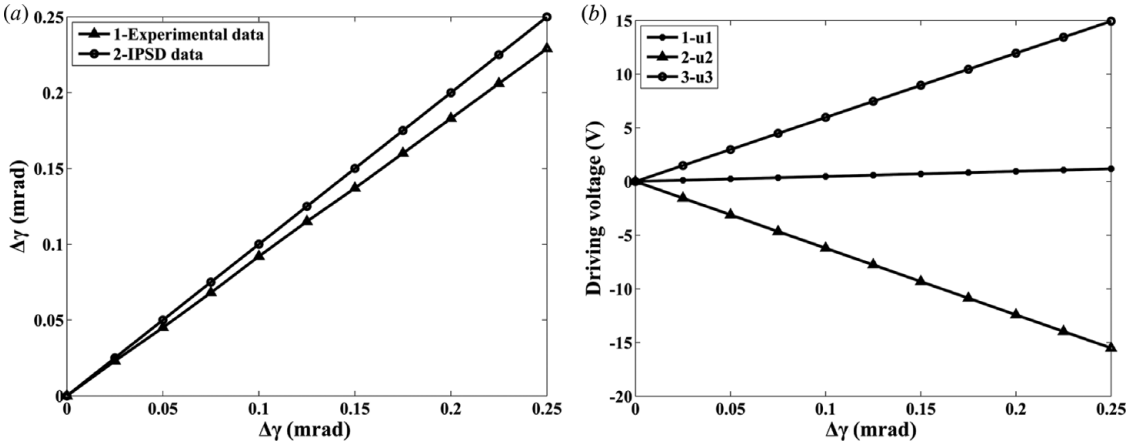


Fig. 17. Comparison of rotation about *Z*-axis between experimental results and IPSD model. (a) Comparison of rotation about *Z*-axis; (b) Relation between driving voltages and $\Delta\gamma$-output.

the errors are relatively large values and can not be neglected, the micromanipulator can not be treated as a fully decoupled $XY\gamma$ manipulator. Considering the generating reasons and the values of errors, we can confirm the accuracy of IPSD model. There are several reasons for these errors, such as modeling errors, actuators errors, manufacture errors, environmental errors, and the errors generated by uncertain pretightening force to each PZT actuator. Because the micromanipulator proposed in this paper is a 3-DOF planar micromanipulator, the manufacture errors and the errors

https://doi.org/10.1017/S0263574711000361 Published online by Cambridge University Press

Table VII. The experimental data and IPSD data when end-effector rotates about *Z*-axis.

$(F^{\mathrm{T}} \quad M_z^{\mathrm{T}})^{\mathrm{T}} = [0 \quad 0 \quad 0]^{\mathrm{T}}$					$\Delta \mathrm{X} = [0 \quad 0 \quad \Delta\gamma]^{\mathrm{T}}$		
Driving voltages (V)			IPSD data (μrad)	Error (%)	The experimental results		
u_1	u_2	u_3	$\Delta\gamma$	$\frac{\lvert\Delta\gamma'-\Delta\gamma\rvert}{\Delta\gamma} \times 100$	$\Delta x'$(nm)	$\Delta y'$(nm)	$\Delta\gamma'$(urad)
0.119	−1.553	1.494	25	8.00	13	−37	23
0.237	−3.105	2.986	50	10.00	27	−72	45
0.355	−4.658	4.480	75	9.33	40	−128	68
0.474	−6.210	5.972	100	8.00	55	−156	92
0.593	−7.760	7.470	125	8.00	65	−165	115
0.711	−9.315	8.959	150	8.67	82	−198	137
0.831	−10.868	10.453	175	8.57	97	−245	160
0.948	−12.420	11.945	200	8.50	111	−293	183
1.066	−13.971	13.439	225	8.44	132	−348	206
1.185	−15.524	14.933	250	8.40	149	−396	229

generated by pretightening force can be eliminated by calibration work. Environmental errors, actuating errors, and modeling errors can be compensated by a fully feedback control system. These questions will be further studied in our future work.

It is also observed that the 3-DOF planar micromanipulator consists of flexure hinges, base, end-effector, and linkages, the IPSD model considers the stiffness of flexure hinges only and regards the other components as rigid body. Thus, the deformation of other components can not be modeled. However, because of calculating efficiency problem, FEM and nonlinear method are not considered as an efficient approach for developing a control strategy for CPM. Only 10 ms is required to complete a calculation of the IPSD model, and Tables II–IV show us the results calculated based on the IPSD model are coincident to the simulational results by FEM. So, the IPSD model can help us to develop a control strategy with full feedback.

9. Conclusions

In this paper, a 3-DOF planar $XY\gamma$ parallel micromanipulator is proposed, and its prototype is developed. The model of relationship among IPSD model is studied. In order to verify the IPSD model, the FEM simulations and experimental testing of the 3-DOF micromanipulator are performed. The main contributions of this paper are as follows:

(1) The $XY\gamma$ parallel micromanipulator has kinematic decoupling characteristic.
(2) The analytical IPSD model is derived. Moreover, the Cartesian stiffness matrix and the driven stiffness matrix of the micromanipulator are obtained, which can be used for investigating the dynamics performance of the micromanipulator.
(3) On the basis of IPSD model, the relationship between driving voltages of PZT actuators and output displacement of end-effector is studied and the analytical expression is given, which is very useful for both digital control and design of the planar micromanipulator.
(4) By using both the simulating technique of FEM and testing method, the correctness and calculating efficiency of IPSD model presented in this paper are verified.

Acknowledgments

This research was supported by the National Natural Science Foundation of China (Grant No:30770538), Major Program of National Natural Science Foundation of China (Grant No:60534020), the Hinge Research Fund for Overseas Natural Science of China(Grant No:50728503), and Doctoral Fund of Ministry of Education of China (Grant No:20060248030).

References

1. J.-P. Merlet, *Parallel Robots* (Kluwer Academic Publishers, London, 2000).
2. L. L. Howell, *Compliant Mechanisms* (Wiley, New York, 2001).
3. F. Scire and C. Teague, "Piezodriven 50 μm range stage with subnanometer resolution," *Rev. Sci. Instrum.* **49**(12), 1735–1741 (1978).
4. J. C. Hudgens and D. Tesar, "A Fully-Parallel Six Degree-of-Freedom Micromanipulator: Kinematic Analysis and Dynamic Model," *Proceedings of the 20th Biennial ASME Mechanisms Conference Trends and Development in Mechanism Machines and Robotics* (1988), vol. 15, pp. 29–37.
5. P. Gao, S.-M. Swei and Z. Yuan, "A new piezodriven precision micropositioning stage utilizing flexure hinges," *J. Nanotechnology* **10**, 394–398 (1999).
6. Y. Li and Q. Xu, "Modeling and performance evaluation of a flexure-based XY parallel micromanipulator," *Mech. Mach. Theory* **44**(12), 2127–2152 (2009).
7. Q. Yao, J. Dong and P. M. Ferreira, "A novel parallel-kinematics mechanisms for integrated, multi-axis nanopositioing Part 1: Kinematics and design for fabrication," *J. Precis. Eng.* **32**, 20–33 (2007).
8. J. Dong, Q. Yao and P. M. Ferreira, "A novel parallel-kinematics mechanisms for integrated, multi-axis nanopositioing Part 2: Dynamics, control and performance analysis," *J. Precis. Eng.* **32**, 7–19 (2007).
9. H.-H. Pham and I.-M. Chen, "Stiffness modeling of flexure parallel mechanism," *J. Precis. Eng.* **29**, 467–478 (2005).

https://doi.org/10.1017/S0263574711000361 Published online by Cambridge University Press

10. X. Tang, I.-M. Chen and Q. Li, "Design and nonlinear modeling of a large-displacement XYZ flexure parallel mechanism with decoupled kinematic structure," *Rev. Sci. Instrum.* **77**, 115101 (2006).
11. Y. Yue, F. Gao, X. Zhao and Q. J. Ge, "Relationship among input-force, payload, stiffness, and displacement of a 3-DOF perpendicular parallel micro-manipulator," *Mech. Mach. Theory* **45**(5), 756–771 (2010).
12. P. Gao and S.-M. Swei, "A six-degree-of-freedom micro-manipulator based on piezoelectric translators," *Nanotechnology* **10**, 447–452 (1999).
13. Y. Yue, F. Gao, X. Zhao and Q. J. Ge, "Relationship among input-force, payload, stiffness, and displacement of a 6-DOF perpendicular parallel micromanipulator," *J. Mech. Robot.* **2**(1): 011007 (2010).
14. G.-J. Chung and K.-B. Choi, "Development of Nano Order Manipulation System Based on 3-PPR Planar Parallel Mechanism," *Proceedings of the 2004 IEEE International Conference on Robotics and Biomimetics, Shenyang, China* (2004), pp. 612–616.
15. T. Lu, D. C. Handley, Y. K. Yong and C. Eales, "A three-DOF compliant micromotion stage with flexure hinges," *J. Ind. robot* **31**(4), 355–361 (2004).
16. Y. K. Yong and T.-F. Lu, "Kinetostatic modeling of 3-RRR Compliant micro-motion stages with flexure hinges," *Mech. Mach. Theory* **44**, 1156–1175 (2009).
17. Y. K. Yong and T.-F. Lu, "The effect of the accuracies of flexure hinge equations on the output compliances of planar micro-motion stages," *Mech. Mach. Theory* **43**, 347–363 (2008).
18. B.-J. Yi, G. B. Chung, H. Y. Na, W. K. Kim and H. Suh, "Design and experiment of a 3-DOF parallel micromechanism utilizing flexure hinges," *IEEE Trans. Robot. Autom.* **19**(4), 604–612 (2003).
19. Q. Xu and Y. Li, "Structure Improvement of an *XY* Flexure Micromanipulator for Micro/Nano Scale Manipulator," *Proceedings of the 17th World Congress IFAC*, Korea (2008), pp. 12733–12738.
20. J. M. Paros and L. Weisbord, "How to design flexure hinges," *Mach. Des.* **37**, 151–156 (1965).
21. S. A. Joshi and L.-W. Tsai, "Jacobian analysis of limited-DOF parallel manipulators," *J. Mech. Des.* **124**, 254–258 (2002).
22. F. Gao, J. Zhang, Y. Chen and Z. Jin, "Development of a New Type 6-DOF Parallel Micro-Manipulator and its Control System," *Proceedings of the 2003 International Conference on Robotics, Intelligent systems and Signal Processing*, (2003) pp.715–720.
23. S. Bandyopadhyay and A. Ghosal, "An algebraic formulation of static isotropy and design of statically isotropic 6–6 Stewart platform manipulators," *Mech. Mach. Theory* **44**(7), 1360–1370 (2009).
24. Z. Huijun and G. Feng, *The Progress of Modern Mechanism* (in Chinese), (Higher Education Press, BeiJing, 2007).
25. S. Vorndran, *The World of Micro-and Nanopositioning 2005/2006* (PI-Polytec Group, Germany, 2005).

https://doi.org/10.1017/S0263574711000361 Published online by Cambridge University Press